



Fan design assessment for BLI propulsion systems

M. Mennicken¹ · D. Schoenweitz¹ · M. Schnoes¹ · R. Schnell¹

Received: 27 March 2020 / Revised: 30 July 2021 / Accepted: 2 August 2021 / Published online: 4 October 2021
© The Author(s) 2021

Abstract

Civil aviation is aiming at fuel efficient aircraft concepts. Propulsion systems using boundary layer ingestion (BLI) are promising to reach this goal. The focus of this study is on the DLR UHBR fan stage of a tube and wing aircraft with rear-integrated engines. In this integration scenario the propulsion system and especially the fan stage receives distorted inflow in steady-state flight conditions. The distortion pattern and distortion intensity are dependent on the operating conditions. Consequently, the interaction of the fan and the distortion changes over the flight envelope. The first part of the paper aims at gaining knowledge of the BLI fan performance in the operating points end of field, approach, cruise (CR) and top of climb (TOC) using high-fidelity, unsteady RANS approaches. The analysis includes fan map performance metrics and a deeper insight into the flow field at CR and TOC. The preliminary design of a fan stage requires fast turn-around times, which are not fulfilled by high-fidelity approaches. Therefore, a fast, throughflow-based methodology is developed, which enables aerodynamicists to design distortion-tolerant fans. The main characteristics of the methodology is outlined in the second part. Consequently, the methodology is taken advantage of to investigate parameter sensitivities in terms of tip speed, blade thickness, solidity, the annulus geometry and a non-axisymmetric stator. This study suggests that distortion-tolerant fans should be designed at higher tip speeds than conventional design experience recommends to limit the local operating point excursion.

Keywords Fan design · Boundary layer ingestion · Total pressure distortion · Distorted inflow

Abbreviations

2D	Two dimensional
3D	Three dimensional
A/C	Aircraft
ACDC	Advanced Compressor Design Code
AP	Approach
BLI	Boundary layer ingestion
CB	Cutback
CR	Cruise
DF	Diffusion factor
DLR	German Aerospace Center
E	Extended
EOF	End of field
ISA	International Standard Atmosphere
LE	Leading edge
MCT	Maximum continuous
MVDR	Meridional velocity density ratio
MTO	Maximum takeoff
OAD	Overall aircraft design

OP	Operating point
RPM	Revolutions per minute
SLC	Streamline curvature
SM	Surge margin
TE	Trailing edge
TOC	Top of climb
UHBR	Ultra-high bypass ratio
(u)RANS	(unsteady) Reynolds averaged Navier–Stokes

List of symbols

A	Area, m ²
a	Specific work, m ² /s ²
c	Velocity in the absolute frame of reference, m/s
d	Blade thickness, m
i	Incidence, °
\dot{m}	Mass flow, kg/s
M	Momentum per second, (kg m)/s ²
MD	Momentum deficit, –
p	Pressure, Pa
s	Chord, m
t	Pitch, m
u	Rotational speed, m/s
w	Velocity in the relative frame of reference, m/s

✉ M. Mennicken
maximilian.mennicken@dlr.de

¹ German Aerospace Center (DLR), Linder Hoehe, Cologne 51147, Germany

Φ	Flow quantity, –
ρ	Density, kg/m ³
σ	Solidity, –
η	Efficiency, –
ω	Angular speed, 1/s
Π_t	Total pressure ratio, –
Π_{t-s}	Total-to-static pressure ratio, –
Indices	
1 or in	Inlet
2 or out	Outlet
ax	Axial
clean	Undistorted inflow
Corr.	Corrected to ISA sea level
is	Isentropic
max	Maximum
Merid.	Meridional
mid-dist	Middle of the distortion
ps	Parameter sensitivity
ref	Reference
u	Circumferential direction

1 Introduction

Aircraft using boundary layer ingesting propulsion systems are expected to be beneficial in terms of increasing overall efficiency [1]. In the literature, recent studies reveal the improvement of the propulsion system in terms of propulsive efficiency as well as mission block fuel burn [2, 3]. Nevertheless, the high degree of integration of the thrust generator in the fuselage results in the necessity of a multidisciplinary design process for such a future aircraft. Especially, the fan rotor has to deal with varying inflow conditions around the circumference. This leads to aerodynamic and structural challenges which need to be faced within the design process. In this paper, the focus is on the fan aerodynamics and, therefore, a short overview of previous research results in this field is given. Moreover, the literature review aims at summarizing the key characteristics of the different fan stages used in those studies. Table 1 lists fan stage characteristics of six different fans. Except of the Whittle Fan, all fan stages are high speed and transonic. Therefore, they are characterized by meridional Mach number and total pressure ratio. As Table 1 reveals, the fans match in meridional Mach number but cover a wide range of total pressure ratios from 1.34 up to 1.70. In contrast, the Whittle fan is a low Mach number fan and, therefore, described by the flow coefficient and the stage loading coefficient. The circumferential Mach number of the Whittle fan rig is 0.13 at a flow coefficient of 0.5 and a stage loading coefficient of 0.47. Gunn et al. [4] compared those numbers with the high-speed VITAL fan stage, which has almost the same stage loading coefficient

Table 1 Fan stage parameters

Fan stage	$\sim Ma_{\text{merid}}$ (–)	φ (–)	Π_t (–)	Ψ (–)
Whittle fan	–	0.50	–	0.47
NASA R4	0.62	–	1.47	–
V2500	0.60	–	1.70	–
Fan 135	0.63	–	1.35	–
BLI2DTF	0.61	–	1.34	–
DLR UHBR	0.60	–	1.31	–

at a higher flow coefficient of 0.65. The Whittle fan is comprehensively investigated in many experimental as well as numerical studies. Gunn et al. [5] investigated BLI flow physics using a 60° distorted sector at a distortion intensity of $DC60 = 0.83$. They experimentally found flow redistribution upstream of the fan stage to significantly change the axial and swirl velocity distribution. In addition, within the distorted sector the rotor tip and stator hub to midspan showed flow separation. In 2014, Gunn et al. [4] applied the boundary layer profile of the silent aircraft initiative (SAI) to the fan stage and discussed the BLI flow physics in comparison to a transonic fan stage. The low speed and high-speed fan revealed comparable BLI flow features only showing differences in the flow details. Two thirds of the additional losses are linked to the rotor and one third to the stator. Perovic et al. [6] carried out an experimental study aiming at stall inception using the boundary layer profile stemming from the Silent Aircraft Initiative and the Whittle fan. The loss in stability limit is between 1 and 2% in flow coefficient. The fan stage is able to operate locally beyond the clean stability limit. Disturbances in static pressure that lead to stall are found to be at lower frequencies than the blade passing frequency. In addition, stall only occurs, if the disturbances can propagate around the circumference. Gunn et al. [7] designed a non-axisymmetric stator for the same integration scenario as presented in [4]. They proved a non-axisymmetric stator to be able to control incidence and blade loading. The stator is less impaired by flow separations and thus the stator shows 10% lower losses than the baseline stator at homogeneous inflow. Moreover, Hall et al. [8] used the Whittle fan BLI data set to calibrate and validate their body force model. Additionally, Hall et al. [8] investigated different fan stages derived from the NASA R4, using their body force approach. The NASA R4 fan stage has a design meridional Mach number of 0.62 at a total pressure ratio of 1.47 [9]. The derived fan rotors differed in radial work input and different axial spacings of rotor and stator as well as a non-axisymmetric stator are applied. Highly loaded fan stages show smaller changes in Diffusion factor around the circumference in rotor and stator compared to the baseline and low loading fans. The hub and tip loaded rotors show similar diffusion factor variations as the baseline in the rotor,

but the stator hub is higher loaded for the tip loaded fan stage and vice versa. The spacing between rotor and stator changes blade loading variations between both rows, while far spaced rotor are higher loaded and stators lower loaded. In close spaced fans it is the other way around. Non-axisymmetric stators reveal bigger variations in diffusion factor and up to 75% the rotor blade loading variations are lower. Only the upper 25% of the rotor blade are higher loaded. Defoe et al. [10] used the body force model approach of Hall et al. [8] to study the influence of boundary layer shape and intensity as well as total temperature distortion effects. The main findings are that changes in diffusion factor are mainly linked to incidence at the inlet velocity triangle. In addition, the diffusion factor changes nearly linear with their stagnation pressure distortion (defined by a velocity ratio) and their stagnation temperature distortion (defined by a total temperature distortion). Another result of their work is the feasibility to superpose different distortions within an error range less than 10%. Schoenweitz et al. [11] assessed the V2500 and the Fan 135 at MTO operating conditions applying a distorted sector with a DC60 of 0.55. The fan stages have a comparable meridional Mach number but differ in total pressure ratio. The V2500 fan stage has the highest total pressure ratio of 1.7 and it is the only fan stage listed in Table 1 used in commercial aero engines. In contrast, the Fan 135 represents a fan stage of an aero engine with a low total pressure ratio of 1.35. It is found that the higher fan pressure ratio fan shows higher flow redistribution effects and a more homogeneous flow field at stator outlet than the low pressure ratio fan. The NASA boundary layer ingesting inlet/distortion-tolerant fan (BLI2DTF) is designed to BLI inflow conditions. The total pressure ratio at ADP is 1.34. Within the fan design process a major focus was on structural integrity (see Cousins et al. [12]). Due to the BLI induced structural challenges the blade thickness distribution was changed compared to the reference blade, which represented a conventional design. They designed a wind tunnel for a coupled nacelle and fan testing. A comprehensive experimental study took place at the NASA Glenn Research Center to measure the complete fan map at BLI conditions [13, 14]. The resulting fan map showed a wide range of stable operating conditions. In addition, at ADP the measured fan efficiency nearly reaches 88%, which is approximately 3% higher than predicted with CFD. In the literature, aircraft concepts are introduced, that have rear mounted fans which ingest parts of the fuselage boundary layer the entire annulus. Pardo et al. [15] assessed a conventional fan design at a low Mach test facility with a total pressure distortion that has the low momentum fluid near the hub of the fan rotor. The clean design showed a radially mismatched rotor due to incidence variations along the span. This resulted in significantly losses in operating range. Then they redesigned the fan stage by aligning the leading edges to the inflow velocity

triangles and adjustments in blade loading. The resulting fan stage has a wider operating range at improved efficiency levels compared to the baseline design. Mårtensson and Laban [16] presented a design and performance assessment study for an aft-propulsor. This propulsor ingests the fuselage boundary layer of a Fokker 100 a/c. They presented the fan map of their design including boundary layer ingestion at ADP and the absence of a fuselage boundary layer at low-speed operation. The realistic total pressure pattern shows also a distortion in the circumferential direction which is not considered in their fan map calculations and needs further studies. Defoe et al. [17] investigated the aero acoustics of coupled intake with the NASA R4 transonic fan stage at BLI conditions. Their findings are a 38dB higher source sound power at low-speed operation, whilst the far-field overall sound power level is only 18 dB higher due to noise-attenuating effects of the inlet duct. Romani et al. [18] determine the aero-acoustic impact of an highly integrated aero engine in a NOVA aircraft configuration. The BLI engine showed higher broad band noise levels of 10–20 dB than the isolated engine. Frequencies above the 2nd BPF show 5–10 dB lower noise levels perpendicular to the engine axis. Additionally, the cumulative noise level is about 18 EPNdB higher at take-off flight procedure from start to cut-back conditions.

The Clean Sky 2 project, the authors are part of, addresses BLI concept studies on the aircraft and the propulsion system level. The overall aircraft design (OAD) includes the assessment of different aircraft designs as well as the integration of the propulsion system. In Fig. 1, two aircraft are highlighted, which are developed by Silberhorn et al. [19]. On the left-hand side in Fig. 1 the baseline aircraft, a standard tube and wing aircraft with under-the-wing-mounted engines, is shown. The aircraft on the right-hand side has buried engines in the rear part of the fuselage, which ingest boundary layer fluid. Further information on the OAD can be found in Silberhorn et al. [19]. The assessment of the propulsion system includes the thermodynamic cycle as well as a detailed fan assessment in different disciplines. A detailed analysis of the engine cycle as well as a coupled engine cycle and fan analysis (zooming approach) can be found in Hollmann et al. [20].

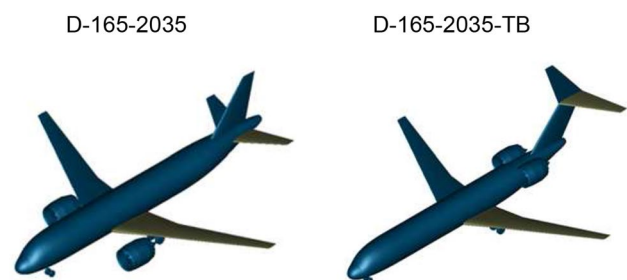


Fig. 1 A/C adopted from Silberhorn et al. [19]

In this paper, the focus is on the aerodynamic performance of the DLR UHBR fan and the paper layout is as follows: first, the DLR UHBR fan will be introduced and assessed in clean as well as four BLI conditions. In comparison to the studies mentioned, the different operating points cover different operating conditions on the flight envelope. Thereafter, the main idea of our new, fast BLI design methodology will be explained. Subsequently, the design methodology will be used to reveal promising design parameters to reach a distortion-tolerant fan design. Both parts, the high-fidelity and the low-fidelity parts, reveal that tip speed is the most important pre-design parameter in terms of a distortion-tolerant fan.

2 DLR UHBR fan performance

In this section, the DLR UHBR fan stage will be investigated. At the beginning, the fan stage will be described. Thereafter, the results of the fan map calculations are presented, which are the reference for the BLI operating conditions. Then, the BLI operating conditions will be presented with a focus on the cruise (CR) and top of climb (TOC) operating conditions.

2.1 General overview of the DLR UHBR

The DLR UHBR fan stage represents a fan for a state-of-the-art aero engine [21]. This fan consists of 22 rotor blades as well as the bypass flow path including 38 outlet guide vanes (OGVs). The core section, including inlet guide vanes (IGVs) for the core or booster, is neglected. One of the design targets of the DLR UHBR was a very high fan face specific mass flow rate of $221 \text{ kg}/(\text{s m}^2)$ in TOC operating conditions ($\Pi_t = 1.45$) resulting in a compact and lightweight engine. The DLR UHBR fan stage is investigated comprehensively, both in numerical as well as experimental studies [21, 22]. At rig scale the fan has a diameter of 0.7 m at the fan face and the fan is tested on the DLR high-speed compressor test facility in Cologne [21, 22]. In the current study, the fan stage is scaled to a fan diameter of 2.34 m to meet the thrust requirements of the given A/C [19, 20]. The cruise operating conditions are set to a meridional Mach number of 0.60 at a total pressure ratio of 1.31 [20]. Compared to the fan stages introduced above the DLR UHBR is in the same range of meridional Mach number but has the lowest total pressure ratio.

2.2 UHBR fan: clean performance

In the following subsections, the assessment of the DLR UHBR comprises homogeneous inflow conditions as for conventional under-the-wing integration scenarios. This

engine integration corresponds to the baseline aircraft, which is shown on the left hand side of Fig. 1.

2.2.1 Numerical setup

Figure 2 shows the flow path of the DLR UHBR fan. The numerical setup consists of the components intake, rotor and stator. A structured OCH mesh topology is applied to all components and the mesh is created by the DLR in-house meshing tool PyMesh. End walls as well as blade surfaces are meshed with $y^+ = 30 \dots 70$. As distance of the first cell is set at a specific blade slice or at a viscous wall, the y^+ value changes with velocity. Typically highest values are reached in the front part of the suction side, where velocity peaks are present. Consequently, wall functions are chosen to those surfaces. This results in 375,000 cells in a rotor passage, 255,000 cells in a stator passage. A quarter of the intake annulus is meshed with 400,000 cells. In the entire control volume, fully turbulent flow is assumed and modeled by the $k-\omega$ Wilcox [23] approach. The extensions for streamline curvature by Bardina et al. [24] as well as the adjustment of entropy production at stagnation points by Kato and Launder [25] are applied to this turbulence model. The fan map calculations at homogeneous inflow conditions are carried out using steady-state single passage calculations. All components are coupled with mixing-planes. A static pressure boundary condition is used as outlet boundary condition at the fan exit. The 3D CFD DLR in-house solver TRACE is used [26].

2.2.2 Fan map

Figure 3 shows the fan map including speed-lines for different shaft speeds as well as operating conditions of the flight envelope. These operating conditions are given by a thermodynamic cycle representing an UHBR engine design with a low total pressure ratio fan and technology assumptions in the timeframe 2035+. Further information on the engine cycle can be found in Hollmann et al. [20]. The surge margin (SM) of the different operating points is assessed according to Cumpsty [27]:

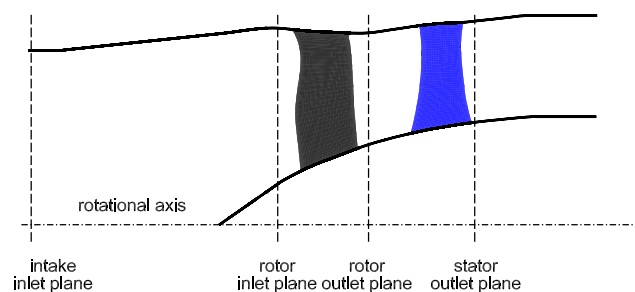


Fig. 2 Flow path of the UHBR fan stage

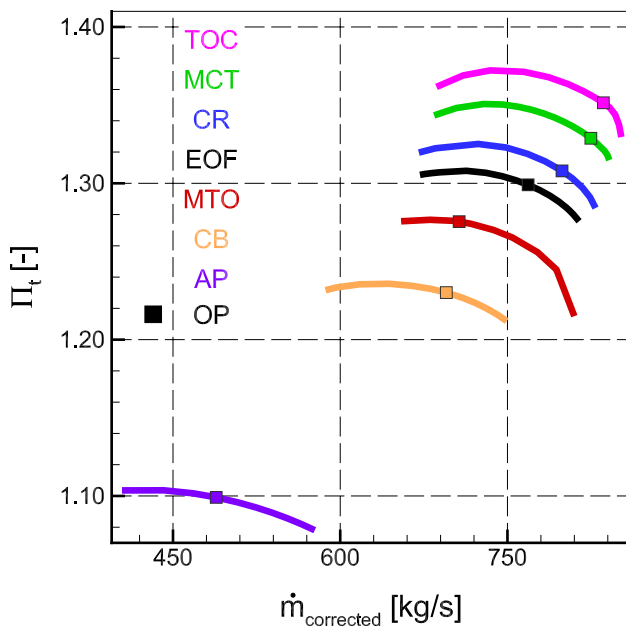


Fig. 3 DLR UHBR fan map

$$SM = 1 - \frac{\Pi_{t,working}}{\Pi_{t,surge}} \cdot \frac{\dot{m}_{surge}}{\dot{m}_{working}} \quad (1)$$

Table 2 shows the results of the operating points for homogeneous inflow. The fan performance data is evaluated from rotor inlet to stator outlet (see Fig. 2). In this study, the operating points of the DLR UHBR fan are shifted to lower fan pressure ratios and meridional Mach numbers compared with the initial design. This results in slight off-design conditions and the fan efficiency decreases marginally. Note that efficiency is normalized by fan efficiency at cruise conditions. In the BLI fan performance assessment, the CR and TOC operating conditions will be analyzed in further detail. Therefore, we take a closer look on clean fan performance in those operating conditions. The left part of Fig. 4 shows the total-to-static pressure ratio characteristic at CR (blue) and TOC (magenta). In the right part of Fig. 4, the normalized total-to-static characteristic is shown, which evaluates the

ratio of the static pressure at the fan outlet (numerator) and the total pressure at the fan inlet (denominator). For the sake of comparability, the characteristics are corrected with the respective operating point. Thus, both operating points are at a corrected mass flow of 1 and a corrected total-to-static pressure ratio of 1. As can be seen in the right part of Fig. 4, the slope of the normalized total-to-static characteristic is steeper at TOC than in CR. This information will be used later to explain the differences in the BLI performance of both operating points. The results presented in this subsection will be used as reference operating conditions in the following subsections.

2.3 BLI fan performance

In this subsection, the fan performance of the aircraft using an embedded propulsion system, which is shown on the right-hand side of Fig. 1, will be addressed.

2.3.1 Numerical setup

In this subsection, the changes compared to the numerical setup for fan map calculations will be addressed. The BLI assessment is carried out using a full annulus 3D unsteady RANS approach. The mesh introduced in Sect. 2.2.1 is used to create the full annulus mesh. As the total pressure distribution due to BLI is a long length scale distortion, the mesh resolution introduced in Sect. 2.2.1 is sufficient to represent

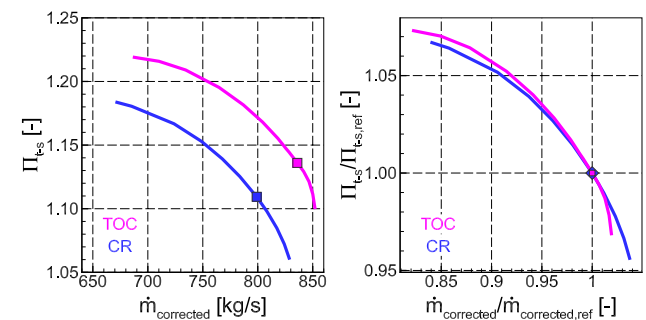


Fig. 4 CR and TOC characteristics of the total pressure ratio (left) and the total to static pressure ratio (right)

Table 2 Fan performance with homogeneous inflow

OP	\dot{m} (kg/s)	\dot{m}_{corr} (kg/s)	Π_t (-)	$\frac{\eta_{is}}{\eta_{is,ref}}$ (%)	SM (%)	RPM (%)
TOC	307.8	836.0	1.3515	99.68	18.52	100.0
MCT	520.8	824.8	1.3288	100.43	17.95	97.4
CR	296.9	799.0	1.3079	100.00	16.82	94.9
EOF	782.5	768.5	1.2990	101.26	13.05	92.4
MTO	693.6	706.7	1.2755	100.33	7.38	88.6
CB	662.6	695.2	1.2301	100.84	15.69	83.1
AP	489.1	488.8	1.0991	100.50	17.63	56.3

the BLI flow features. Additionally, the paper by Schnell et al. [22] includes the analysis of different grid levels for the UHBR fan stage. A second-order Euler backward approach for time discretization is used. The coupling of the components is made using non-sliding 1:1 interfaces according to Yang et al. [28]. The total pressure distributions at different flight conditions, which are used within the inlet boundary conditions, are provided by 3D aircraft CFD results [29, 30]. In the next subsection, the characterization of these distortions takes place and the total pressure distribution is shown in Fig. 5. The selection of a proper operating point is an often-discussed topic in the context of BLI. Engines dealing with clean inflow generally have a choked bypass nozzle. So, the operating point can be determined by finding a point on the nozzle characteristic that fulfills the thrust requirement. In BLI engine integration scenarios, additional difficulties come into play. First, the thrust requirement of a BLI a/c is not necessarily equal to the reference a/c. Second, the fuselage geometry downstream of the nozzle could affect the static pressure distribution in the nozzle. This in turn would lead to a different nozzle characteristic. As we do not have the information about thrust requirement and downstream installation effects as well as the nozzle is excluded from the numerical setup, we need to take an assumption for the BLI calculations. In the authors view, there are two options to carry out the BLI calculations. The first option is to maintain the same static pressure at fan stage exit. This mainly keeps the operating conditions of the undistorted passages unchanged, whilst the passages in the distortion operate shifted towards the stability limit. The mass flow rate is expected to be lower compared to the non-BLI engine due to the momentum deficit of the ingested boundary layer. The total pressure ratio will increase but in general the thrust requirement of the non-BLI a/c cannot be matched either. The resulting fan performance is expected to change to higher fan pressure ratios and lower fan efficiencies. The margin to the stability limit is expected to be reduced. The second option is to find an operating point that is on the

nozzle characteristic. Assuming the same nozzle area, the nozzle characteristic will have a slightly different slope in the fan map due to lower total pressure at engine inlet. However, the authors expect to achieve a matching with the nozzle characteristic by increasing the mass flow of the fan. This is at the expense of the non-distorted passages of the fan, which will work in choking conditions. So, this resulting operating point would have lower fan efficiencies than the reference point. Schoenweitz et al. [11] used the approach of option one and Gunn et al. [4] simplified the approach of the second option. The interaction of the distortion with the fan and the resulting BLI flow physics are comparable for both approaches. The authors expect distortion-tolerant fans to operate at non-choking conditions in the non-distorted passages around the circumference. This would require adjustments of the nozzle. For the sake of simplicity and in the awareness of the simplifications, we decided to take the first option. So the static pressure at fan stage exit is kept constant compared to the reference operating points.

2.3.2 Characterization of the distortions

The BLI fan performance is assessed at the four different operating conditions CR, TOC, AP and EOF. The TOC operating point is chosen due to the highest total pressure ratio. CR conditions represent the largest part of a common flight mission. EOF as well as AP is relevant in the context of aero-acoustics. Figure 5 shows the non-dimensional total pressure distribution at the four flight conditions of the four mentioned operating points [29, 30]. The CR and TOC boundary condition are the same due to the definition of these operating conditions. Both are defined at the same altitude and flight Mach number. The approach and the EOF operating conditions differ compared to the CR/TOC operating conditions and the non-dimensional total pressure distribution is more homogeneous than in CR/TOC. As the momentum deficit, which is present in the approaching boundary layer fluid, is the main driver in terms of improving the overall engine performance, we introduce a metric, which accounts for the momentum deficit per second (MD). MD is calculated at intake inlet using Eq. 2, where M is the arithmetic product of the density ρ , the square of the speed c^2 and the area A ($M = \int \rho \cdot c^2 dA$):

$$MD = \frac{M_{\text{clean}} - M_{\text{BLI}}}{M_{\text{clean}}} \quad (2)$$

The CR and TOC conditions are exposed to a momentum deficit of 5.5%. This is relatively high compared to 2.28% and 1.60% in approach and EOF, respectively. Therefore, the cruise and TOC operating conditions are expected to have the greatest changes in BLI operating conditions compared to the homogeneous inflow.

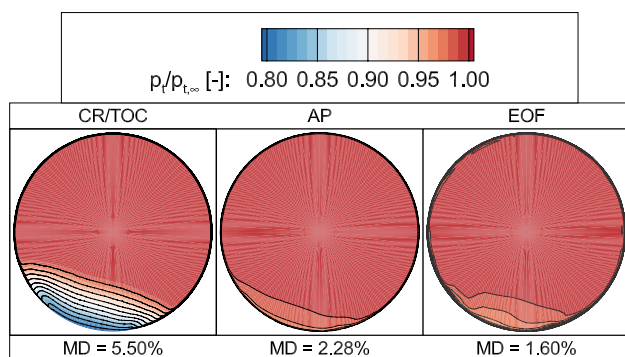


Fig. 5 Non-dimensional total pressure distribution at different flight conditions resulting from A/C CFD [29, 30]

Table 3 Changes in BLI fan performance compared to clean inflow

OP	\dot{m} (%)	\dot{m}_{corr} (%)	Π_t (%)	$\eta_{is}/\eta_{is,ref}$ (%)
TOC	-2.44	-1.24	+0.04	-1.48
CR	-3.60	-2.10	+0.28	-1.91
EOF	-0.51	-0.18	+0.11	-0.25
AP	-0.33	-0.16	+0.05	-0.18

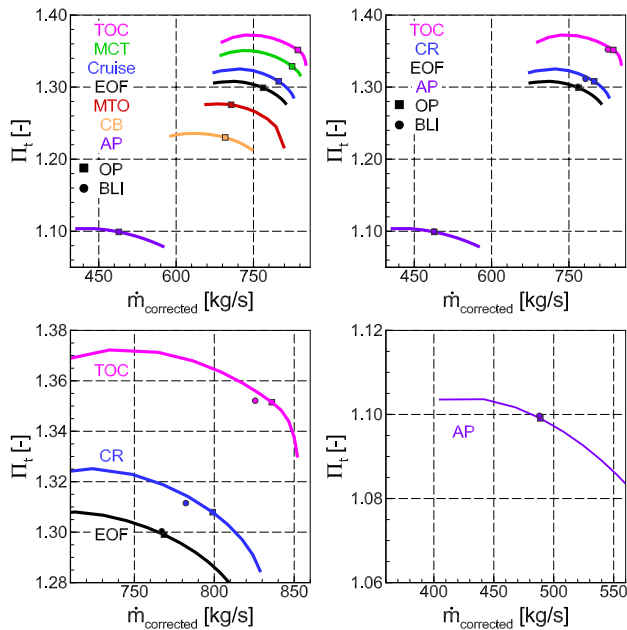


Fig. 6 Reference fan map (upper left), fan map including the BLI OPs of the 4 BLI conditions (upper right) and two zooms in the BLI fan map (lower left and right)

2.3.3 Changes in the fan map

Table 3 shows the relative changes in fan performance compared to the respective clean reference operating conditions. The performance parameters change for all operating conditions in the same way. Mass flow as well as corrected mass flow decreases, total pressure ratio increases and the fan efficiency drops. The resulting operating points are shown in the fan map in Fig. 6. Those changes are larger in CR and TOC operating points as in the AP and EOF operating conditions. At AP and EOF, the variation of non-dimensional total pressure caused by BLI is smaller and, therefore, the changes in fan performance are also small. The greatest decline in (corrected) mass flow is observed in CR. Moreover, this operating point has the biggest increase in fan pressure ratio.

As CR and TOC operate at the same total pressure distribution, the question arises why the fan behavior differs between both OPs. The answer to this question can be found by investigating the steepness of the total-to-static characteristics. As Fig. 5 revealed, the TOC OP has a steeper

total-to-static pressure ratio characteristic. In the BLI calculations we assume the same static backpressure as at the reference point. Moreover, at stator exit the static pressure is homogeneous as long as the stator provides a swirl free outflow. Even in BLI conditions the stator can provide such conditions. So in the evaluation of the total-to-static characteristic, the denominator is constant but not the numerator due to the boundary layer. Consequently, the fraction of total pressure at the fan inlet and the static pressure at the fan exit increases inside of the boundary layer. Those throttled conditions are found at lower mass flow conditions and the steepness of the characteristic accounts for the amount of operating point excursion. If the characteristic is steep, the BLI operating point in terms of mass flow is found near the reference point. This is true for TOC. The opposite case leads to a large shift in terms of mass flow as we have seen in CR conditions. As the operating point in terms of mass flow is fixed, the other changes in performance quantities (i.e. total pressure ratio, efficiency, etc.) follow their respective characteristics. In the specific case the characteristics at TOC help conserving fan performance. When the fan stage and the intake are assessed in cruise conditions the average drop in isentropic efficiency amounts for approximately 1.6%. This value is used in the OAD level to take the drop of overall engine efficiency into account. The investigation of the A/C including the fan performance degradation can be found in Silberhorn et al. [19].

2.3.4 Comparison BLI vs. clean flow

In this part, the focus is on the differences between the clean inflow and BLI inflow conditions at CR and TOC operating conditions. Figure 2 shows a part of the flow path of the DLR UHBR fan stage. The fan rotates counterclockwise looking in the direction of the flow. The following plots show flow quantities in so-called S3 planes. The primitive flow quantities are evaluated at the rotor inlet plane and the relations of the rotor are evaluated between the rotor inlet and outlet plane (see Fig. 2). To support the orientation we will name different circumferential positions with the help of a clock and the middle of the distortion is located in the 7 o'clock position. First, the flow redistribution in front of the rotor due to BLI is compared between both operating points. The flow fields in Figs. 7, 8, 9 and 11 show the differences of different flow quantities caused by BLI compared to clean inflow. Those changes are evaluated using Eq. 3.

$$\Delta\Phi = \Phi_{BLI} - \Phi_{clean} \tag{3}$$

As we have seen in the section above, in the 0D fan performance the decrease of mass flow is higher in CR than in TOC. As a first-order effect, the reduction in mass flow translates in reduced axial velocity in front of the rotor.

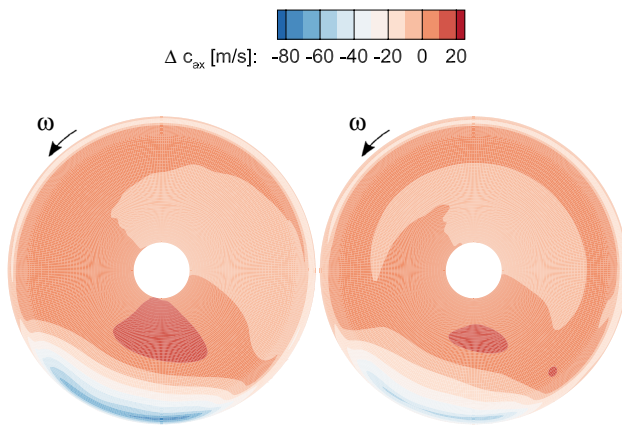


Fig. 7 Axial velocity delta CR (left) and TOC (right)

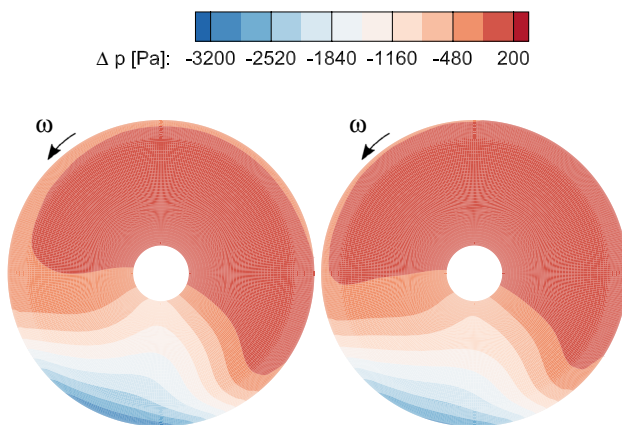


Fig. 8 Delta static pressure CR (left) and TOC (right)

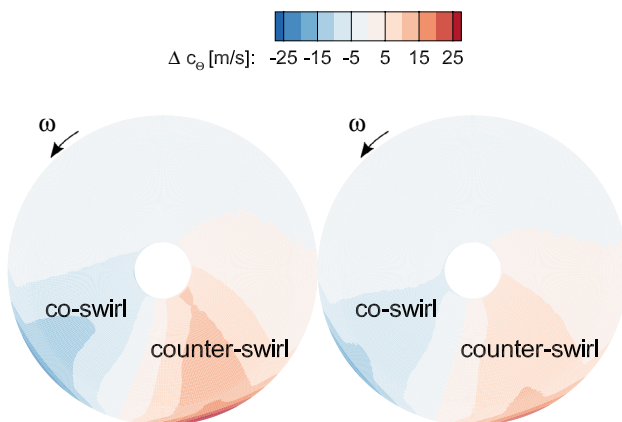


Fig. 9 Swirl in front of the rotor visualized by Δc_θ for CR (left) and TOC (right)

Figure 7 shows these differences in axial velocities for CR (left) and TOC (right) operating points. Phenomenologically both plots show equal effects but as the mass flow reduction indicates, these changes are higher for cruise. In addition,

the changes in axial velocity and consequently in Mach number lead to variations of the static pressure field in front of the rotor, which are visualized in Fig. 8. Both static pressure plots show the same shape but the variations in static pressure are higher for cruise. Note that both OP have different mass flows in homogeneous conditions but the total pressure at the inlet is the same. This leads to different Mach numbers at the rotor inlet and, therefore, different levels of static pressure. The static pressure distribution indicates that there are static pressure gradients in front of the rotor. These static pressure gradients induce swirl to the flow. The swirl in the absolute frame of reference is shown in Fig. 9. By the similarity of the static pressure field, the induced circumferential velocity distributions look similar. Highest values of circumferential velocities are in regimes, co- and counter-swirl, located in the tip region. Moreover, the velocity distributions show that the changes in axial velocity are an order of magnitude larger than these of the circumferential velocity. The inflow velocity field points out the continuously changing conditions the fan has to deal with during each rotation. These changes are commonly evaluated by the rotor incidence. The homogeneous inflow conditions are taken as reference and these conditions are defined as zero incidence. These flow redistribution effects are in line with those found in Gunn et al. [5], Gunn et al. [4], Hall et al. [8], Schoenweitz et al. [11] and Arend et al. [13]. In Fig. 10 the spanwise incidence distributions are plotted at five circumferential positions in CR (upper) and TOC (lower). Moreover, the maximum positive incidence, which is found in near stall condition for homogeneous inflow, is represented by the dashed line for both OPs. In steady TOC conditions slightly higher values of maximum positive incidence can be handled than in CR. The perceived behavior of the different circumferential positions is similar in CR as well as TOC BLI conditions. Far away from the distortion, in passage 1, no incidence occurs. The co-swirl in passage 15 leads to negative incidence at the full span. In passage 13 the axial velocity decreases in the boundary layer and positive incidence is observed at full span. The passages 10 and 11 show slightly negative incidences near the hub and at midspan. This is due to slightly increased axial velocities. In passage 11 the highest positive incidence in the tip region is observed. Incidence reduces in passage 10 due to increased axial velocity though counter-swirl is present. Comparable incidence distributions are presented by Gunn et al. [4]. Note that the positive incidences above 80% span of the passages 10, 11 and 13 are far beyond the stable operating conditions with homogeneous inflow. In line with the bigger reductions in axial velocity in CR, the highest positive incidences occur in CR. In both OPs the variation of incidences near the hub are small compared to the incidences in the tip region. The stability of the fan is not impaired even though some radial parts of the fan operate locally outside the stable area. Two effects help to

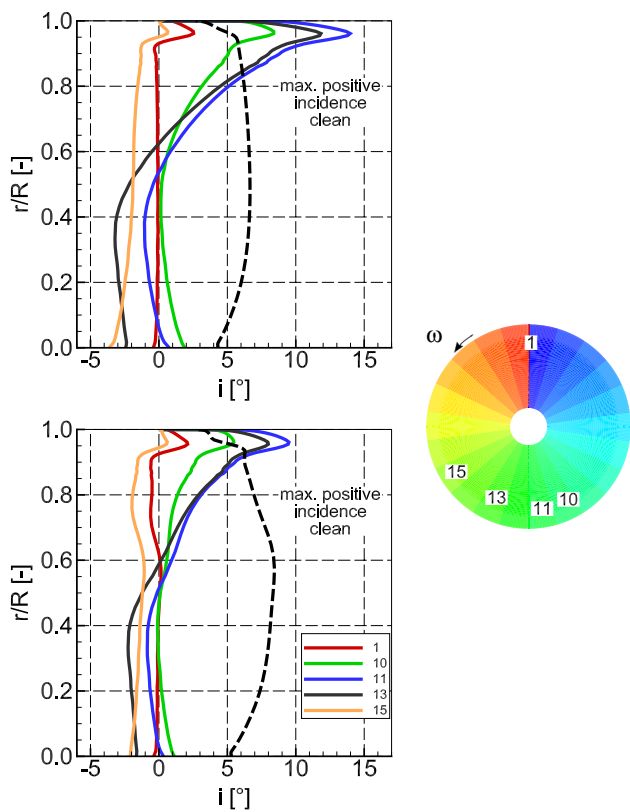


Fig. 10 Spanwise incidence CR (upper) and TOC (lower). The dashed lines show the incidence at the stability limit at clean inflow

preserve the fans stability: on the one hand, the radial distribution of the flow through the fan blade differs in BLI conditions compared to the conditions at the stability limit at clean inflow. The small portion of the radial height is kept stable due to the rebalanced flow in the blade passage. On the other hand, the fan blade has to deal with unfavorable conditions only at a small portion of the annulus. In between, the flow field of a blade passage can recover while the fan blade is rotating in higher momentum fluid (see Perovic et al. [6]). The variation of rotor incidence leads to variations in work input around the circumference. Therefore, the total pressure ratio changes in the BLI case compared to homogeneous inflow. Figure 11 shows the difference of the clean and BLI total pressure ratio in cruise (left) and TOC (right) operating point. Both patterns are similar but the absolute values of the changes are different. In the 1 o'clock position, the fan is in the opposite circumferential position compared to the boundary layer. As can be seen there, the fan operates as in homogeneous inflow conditions. As the fan rotates counter-clockwise, the total pressure ratio drops in the co-swirl area, which is located in the 9 o'clock position. Thereafter, the fan enters the boundary layer fluid and the fan pressure ratio rises to its peak near the 6 o'clock position, which is located in the counter-swirl area. Thereafter, the total pressure ratio

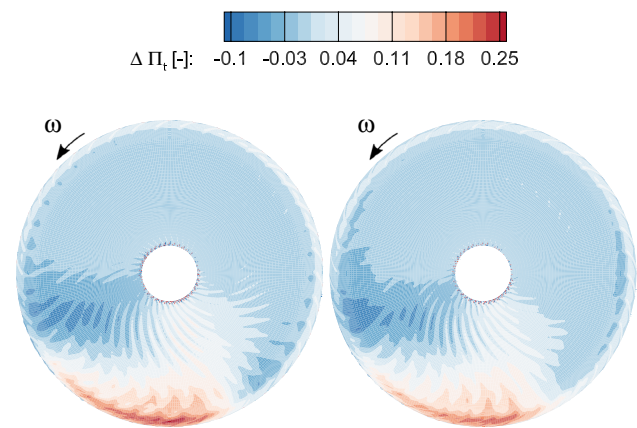


Fig. 11 Delta total pressure ratio for CR (left) and TOC (right)

decreases until comparable inflow conditions are reached as in the reference operating point. The Cruise operating point shows higher increases of total pressure ratio in the boundary layer, what is in line with the findings of the averaged operating points in the fan map.

3 BLI design methodology

The unsteady RANS approach, which is the state-of-the-art approach to capture BLI flow physics, requires a full annulus computational domain. The calculation of a BLI flow field takes approximately 8000 CPUh even if meshes are applied, which use wall functions. Therefore, the full annulus uRANS approach is not suitable for a high number of design iterations, which are commonly necessary at pre-design level. Nevertheless, the uRANS approach remains essential to assess a specific fan design at a later stage in the design process. So far, the BLI assessment requires a lot of computational effort. To overcome this weakness in the BLI design process we outline a new design methodology, which is comprehensively described in Mennicken et al. [31]. The backbone of the new design methodology is the in-house throughflow code ACDC, which is based on the streamline curvature approach (2D SLC) [32]. In general, the throughflow approach results in a circumferentially averaged flow field in an axial-radial plane. ACDC has a database of optimal airfoils included, which is queried at every design run. The major benefit of having the airfoil database is that at the end of every design run 3D blade geometries are available. Those can be taken advantage of in higher fidelity assessment as well as in other disciplines like in structural mechanics. The new design methodology consists of two steps: Firstly, a fan design is carried out using ACDC. In this step we apply homogeneous inflow boundary conditions and, therefore, this step is mainly the same as in conventional non-BLI designs. Secondly, the fan design can be assessed in

the BLI scenario. Note that this is the key feature of the new design methodology. The design assessment required some extensions and calibrations to be made in the throughflow approach, which results in the extended SLC approach (2D E-SLC). As presented in the previous sections, in the BLI scenario the interaction of the boundary layer and the fan stage takes place in front of the rotor. This results in flow features in the circumferential direction. These are swirl due to static pressure gradients and an acceleration of the boundary layer fluid due to stream tube contraction (also driven by the static pressure gradients). The new design methodology is required to reproduce those flow features to provide an appropriate fan performance prediction. The methodology is able to represent the velocity deficit due to boundary layer ingestion. Incorporating the extension and having them calibrated the stream tube contraction and swirl in front of the rotor is included. Obviously, the limitations of throughflow approaches remain. The friction between solid surfaces and the fluid is not resolved. In addition, shock structures in transonic flow regimes are accounted for but as shock systems are three-dimensional, a two-dimensional approach is limited in reproducing this effect. Nevertheless, within the study presented in [31], the new design methodology is validated by the comparison of the high fidelity and low fidelity results of three specific fan designs, which are obviously not part of the calibration data set. The biggest differences were present for the ascending fan design. The results for constant and descending fan pressure ratio showed less variations between the approaches, but to give the reader an idea of the highest amount of variations between high fidelity and pre-design the ascending fan design is best suited. The changes in fan pressure ratio around the circumference (between the clean and the distorted passage) were 0.08. The difference between the uRANS and 2D E-SLC approach in distorted inflow conditions showed a difference of 0.025 over the entire span. The pre-design methodology underestimated, i.e. the effect of unsteady work input due to BLI. The diffusion factor at 80% span varies about 0.037 between clean and distorted inflow, whilst the changes between the approaches in distorted inflow is 0.051. The pre-design methodology overestimates the changes in blade loading due to BLI. This is partly caused by the one-dimensional stream tube contraction model, which implies to trade hub vs. tip flow. Consequently, the velocity triangles overestimate axial velocity near the hub and at the tip the axial velocity is a too low. This in turn leads to bigger variations in the diffusion factor. Nevertheless, the shape of the radial DF distribution and the increase of DF due to BLI are well reproduced. So, the design methodology is limited in terms of not revealing the exact value in the DF changes. However, as the trends between different designs are well represented and the changes are overestimated, the assessment using the design methodology is conservative natured.

In Fig. 12, the flowchart shows the main idea of the BLI assessment in the 2D E-SLC approach. First, a number of passages around the circumference needs to be defined. In every passage, the total pressure distribution at the inlet is given by the boundary layer distribution. Moreover, the swirl distribution as well as the stream tube contraction modelling need to be set. Those distributions are based on a calibration data set as described in Mennicken et al. [31]. In contrast to the BLI assessment presented above, a generic boundary layer based on turbulent flat plate assumptions [33] is applied. Every passage requires a single throughflow calculation and in the end the aerodynamicist has a number of flow fields available to assess the specific fan design. The entire design and BLI assessment take approximately 0.008 CPUh, which translates into a few seconds on an ordinary workstation. Summarizing the major advantage of the BLI design methodology is the availability of a BLI assessment at conceptual design level with low turnaround times. Thus, this approach enables to run a high number of design iterations, which are required at conceptual design level.

4 Fan stage design parameter sensitivities

In this section, we will investigate the influence of different design parameters on BLI fan performance and take advantage of the newly developed design methodology. The DLR UHBR fan stage, which has been assessed in Sect. 2, forms the basis for the following investigations. In this sensitivity study, the rotor tip diameter retains fixed as this is associated with a given installation space and to a comparable ratio of the fan diameter to the fuselage boundary layer height. In addition, the design philosophy of the fan stage retains constant within this study, which manifests in a fixed design

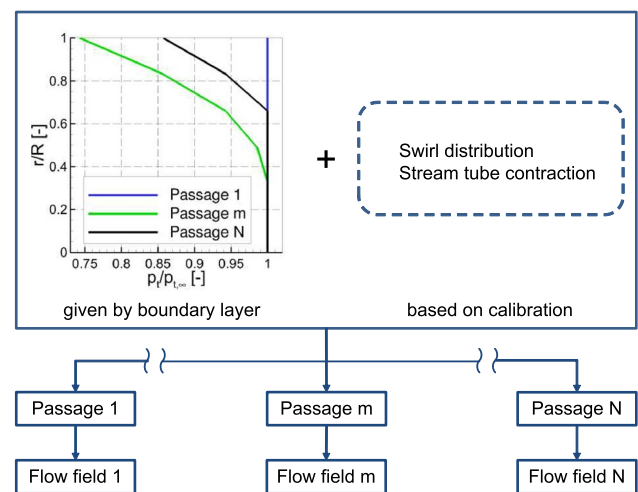


Fig. 12 Flowchart BLI assessment in 2D E-SLC

mass flow, total pressure ratio and radial work input. The sensitivity study is conducted as follows: first, three designs with varying tip speed will be introduced. These designs subsequently serve as references for the further design parameters that will be examined. This opens up a design space, in which the impact of the design parameters can be observed. In the authors view, it is very important to observe the impact of the design parameters in this design space to eliminate the risk, that a design parameter only behaves for a given fan stage set in a certain way. Secondly, the sensitivities of a changed rotor blade thickness, rotor solidity, rotor tip line and a non-axisymmetric stator are investigated for these three tip speeds. The authors expect the rotor design to be the more challenging part in designing a distortion tolerant fan. For that reason, mainly, the design sensitivities are linked to rotor design parameters. Nevertheless, the sensitivity of a non-axisymmetric stator is also investigated.

4.1 Fan performance metrics

Before introducing the design sensitivities, we will define the metrics for assessing the fan performance. As propulsion units are required to be as efficiently as possible, we use Eq. 4 to assess the isentropic efficiency of the parameter sensitivities compared to the reference designs (varying in tip speed) at clean inflow conditions:

$$\Delta\eta_{is, clean} = \eta_{is, ps} - \eta_{is, ref} \tag{4}$$

This procedure is important to separate the impact of a specific design parameter from the impact of the tip speed. In addition, the changes in isentropic efficiency due to BLI are important to evaluate and, therefore, we use Eq. 5:

$$\Delta\eta_{is} = \eta_{is, mid-dist} - \eta_{is, clean} \tag{5}$$

Beside efficiency, stable engine operation is a must for aviation propulsion. As it is beyond the scope of this paper to judge entire engine operation, we aim at assessing the aerodynamic blade loading and for that reason we use the diffusion factor (DF) defined in Eq. 6. This metric includes the summand w_2/w_1 (known as deHaller number), which accounts for the flow deceleration and a summand, that accounts for the flow turning. The flow turning part also includes geometric input via the chord to pitch ratio (solidity σ):

$$DF = 1 - \frac{w_2}{w_1} + \frac{\Delta w_u}{2 \cdot w_1 \cdot \sigma} \tag{6}$$

The changes in the diffusion factor are assessed around the circumference at 80% rotor span using Eq. 7:

$$\Delta DF = DF_{mid-dist} - DF_{clean} \tag{7}$$

As DF is highly linked to velocity triangles and, therefore, to the flow field, a high value of ΔDF is considered to be linked to high unsteady changes in blade loading. Positive values of ΔDF indicate that the fan blade operating conditions are shifted towards the stability limit. Nevertheless, it should be kept in mind that there is always an individual, blade-dependent value of the Diffusion Factor at the stability limit. Therefore, this criterion can just be used in a qualitative manner. Those design metrics are in line with the performance assessment carried out in [31].

Figures 16 and 17 show the results of the sensitivity study and will be discussed during the course of this section. The results of the clean performance analysis are shown in Fig. 13.

4.2 Tip speed

In this part, we analyse fans with three different ISA-corrected tip speeds, which have been introduced in [31]. The DLR UHBR fan stage evaluated in Sect. 3 has a tip speed of 284 m/s. In addition, higher tip speeds of 307 m/s and 328 m/s will be investigated. Equation 8 gives the work input in the fluid and is well known as Euler’s turbine equation:

$$a = u_2 \cdot c_{u,2} - u_1 \cdot c_{u,1} \tag{8}$$

According to this equation the work input depends on the rotational velocity of the blade u and the circumferential velocity component of the velocity in the absolute frame of reference c_u at inlet (1) and outlet (2). Figure 16 shows velocity triangles at rotor in- and outlet. As the radial total pressure ratio and, therefore, span wise work input is fixed in this study, increasing tip speed leads to decreasing flow turning and vice versa. As already shown in [31], the fan characteristic steepens up with increasing tip speed. In addition, the total-to-static pressure characteristic is steeper for fans with a higher tip speed. Increasing the tip speed from 284 to 307 m/s leads to decreasing fan efficiency of $\sim 0.1\%$ at clean inflow conditions. A further increase from 307 to 328 m/s

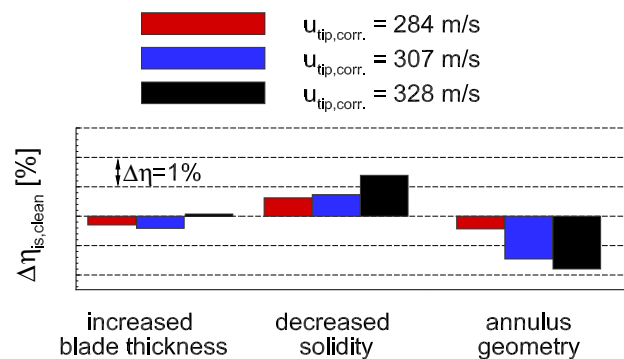


Fig. 13 Isentropic efficiency of the design sensitivities at clean inflow

results in an additional efficiency drop of $\sim 1.3\%$. Figure 15a shows the DF for homogeneous inflow. Tip speed has a direct impact on DF. The solidity of the three designs is constant and, therefore, the changes in DF stem from changes in the velocity triangles at rotor in- and outlet. For compressor blades, the designer tends to increase the tip speed while aiming at lower aerodynamic blade loading. Above 30% span, DF shows the expected behavior. On the one hand, the flow turning assessed by Δw_u is higher at lower tip speeds according to the explanation given above. On the other hand, the inflow velocity w_1 decreases at those conditions. Nevertheless, both effects taken together lead to an increased flow turning term, if tip speed decreases. As a result, we observe that the deHaller number (deHaller = $\frac{w_2}{w_1}$) decreases with decreasing tip speed. Taking the outflow velocity triangle into account an increased deHaller number leads to an increased $c_{u,2}$ velocity component, which is required for the work input. Summarizing both effects lead to higher DF in the rotor. The hub flow in fan blades shows a counterintuitive behaviour. Below 30% span, the trend changes and the design with lowest tip speed shows lowest aerodynamic blade loading. As discussed above the work input depends on u and $c_{u,2}$. First, near the hub the fan with lowest tip speed requires a high $c_{u,2}$, which only can be reached by a stagger angle smaller than 90° . This leads to a velocity triangle at rotor outlet in which all velocity components have the same direction in regard of their circumferential component and increase $c_{u,2}$. Secondly, an accelerating airfoil (associated with a deHaller number above unity) also increases $c_{u,2}$. Both effects are true for the lowest tip speed and lead to very low values of DF. These trends remain at BLI conditions. Figure 15b shows the spanwise DF in the middle of the distortion. As the total pressure distortion is located in the tip region of the blade and extends to midspan, the hub flow is comparable to clean inflow conditions. So, there are only minor changes in DF compared to clean inflow conditions. In the spanwise positions the boundary layer fluid is located, the aerodynamic blade loading increases. The boundary layer fluid is represented by decreased axial velocity. This has two implications. Firstly, the decrease in axial velocity leads to a lower relative inflow velocity w_1 . Secondly, the fan has to deal with positive incidence and the flow turning in the rotor increases. Both effects lead to an increasing blade loading. The steepness of the characteristic determines the operating point excursion, as in the middle of the distortion a specific value on the characteristic needs to be matched to meet the flow field at stator exit. We have already seen this phenomenon in Sect. 2. This leads to a lower operating point excursion in terms of mass flow with increasing tip speed.

The design with lowest tip speed shows highest changes in isentropic efficiency of -0.47% and an increase of ΔDF

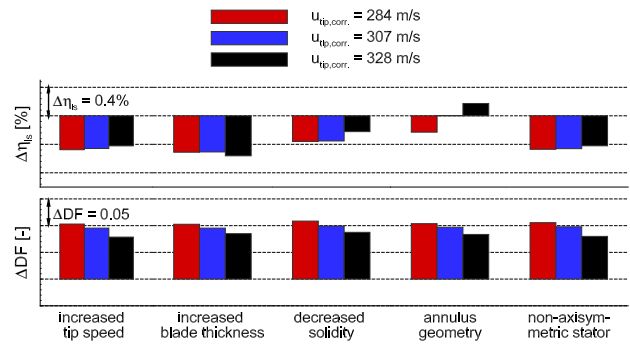


Fig. 14 Changes between the passages outside of the distortion and in the middle of the distortion. Upper: isentropic efficiency. Lower: diffusion factor

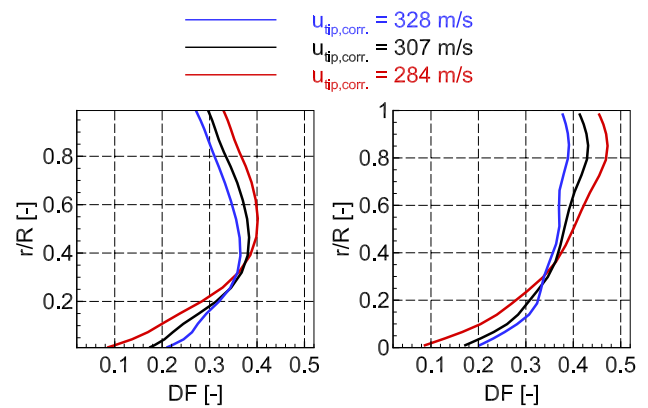


Fig. 15 Spanwise diffusion factor in the rotor for homogeneous inflow (left) and in the middle of the boundary layer (right)

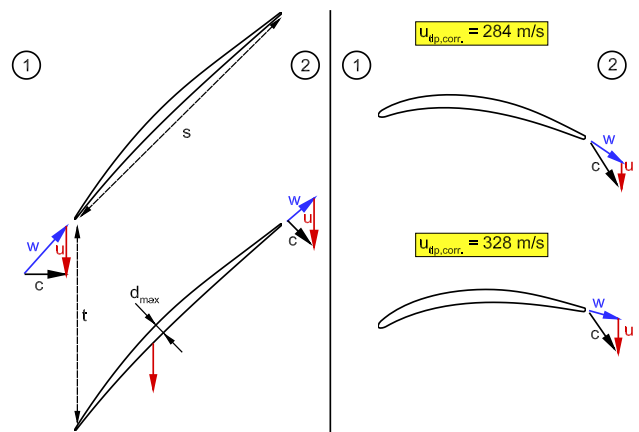


Fig. 16 Left: blade-to-blade view of a rotor passage including inflow and outflow velocity triangles as well as chord length s , pitch t and airfoil thickness d_{max} . Right: rotor outflow velocity triangles at the hub for different rotational speeds

of 0.103 at 80% span (see Fig. 14). Figure 14 also reveals that as the tip speed increases the efficiency drop decreases to -0.46% or -0.42% , respectively. In addition, blade loading variations get smaller and ΔDF is 0.095 or 0.079, respectively.

4.3 Blade thickness

In the literature, there is only one specific BLI fan design reported by Cousins et al. [12]. In their design, the blades are thickened to support mechanical integrity of the fan rotor. Note that proving the mechanical integrity of the fan blades (forced response, flutter, etc.) is beyond the scope of this paper and the focus is rather on the aerodynamic performance assessment. Further information on that topic can be found in Eichner et al. [34].

In general, thicker blades are expected to have degradations in fan performance and this design iteration aims at a quantification of this impact. In this parameter sensitivity the parameter blade thickness normalized by the chord length is increased by approximately 2% compared to the reference blades. In undistorted inflow conditions the increased blade thickness in the rotor leads to slightly lower fan efficiencies for the fan stages with corrected tip speeds of 284 m/s and 307 m/s. The 284 m/s case has an efficiency loss of -0.28% and the 307 m/s case has a lower efficiency of -0.38% . Only the fan stage with a corrected tip speed of 328 m/s shows a 0.07% higher isentropic efficiency at clean inflow. Therefore, we can conclude that the reference design for the highest tip speed has some potentials for a better profile selection. In BLI conditions the changes in isentropic efficiency show a different trend tending to higher efficiency losses with increasing tip speed. As the blades get thicker, choke margin is reduced. As the stream tube contraction locally increases inflow velocities at midspan, those regions are locally pushed into choking conditions. Thus, isentropic efficiency further decreases in the middle of the distortion. The low and intermediate tip speed show the same efficiency loss of -0.51% and the highest tip speed fan has an efficiency loss of -0.56% . The changes in blade thickness cause only minor changes in ΔDF at 80% span. The changes of ΔDF are 0.103, 0.095 and 0.085 with increasing tip speed. The main message from this subsection is, that the blade thickness obviously has an impact on fan performance. The database of optimized airfoils used in this study showed the ability to limit the detrimental effect of thicker fan blades largely.

4.4 Decreasing solidity

In the next parameter sensitivity, the blade count in the rotor is decreased. The solidity σ is a measure that evaluates the ratio of chord and pitch ($\sigma = \frac{\text{chord}}{\text{pitch}} = \frac{s}{t}$). Figure 16 shows the

geometry parameters pitch t and chord s . As the chord length is fixed, the reduction of 4 blades in the rotor blade count transfers in approximately 20% lower solidity along the rotor span. This results in higher values of the diffusion factor as solidity has a direct impact on the flow turning term. While the deHaller number is unaffected by the change in clean and distorted inflow, the diffusion factor increases due to the changes in solidity. At clean inflow conditions, the diffusion factor increases at 80% span about 6.4% for lowest tip, 5.7% with the intermediate tip speed and 4.1% for the design with highest tip speed. On the one hand, decreasing solidity leads to a bigger area enclosed by the isentropic Mach number distribution. So, the flow deceleration along the blade as well as pre-shock Mach numbers increase. Those effects cannot be disclosed directly by the applied approach, but the data base of optimised airfoils includes this information. On the other hand, the amount of wetted area is lower with decreased blade count. All in all, the here examined parameter sensitivity has, as expected, a high impact on fan efficiency at clean inflow. This is due to lower viscous losses caused by the lower count of rotor blades and less blade wakes. The efficiency gain increases from 0.58%, 0.67% or 1.27% with increasing tip speeds, respectively. This leads to the judgement that the fan is over bladed or has a chord length that is too long, if only the cruise conditions are considered. Commonly off-design conditions, which are located near the stability limit demand for higher blade counts or higher chord lengths. This is true for the initial DLR UHBR fan design, which operates at take-off conditions near the stability limit. Specifically, the scaled DLR UHBR fan has to deal with operating conditions a near the stability limit at MTO, as shown in Fig. 4 in Sect. 2. Taking the BLI conditions into account the diffusion factor is higher in the middle of the distortion compared to the baseline cases. The same explanation as given above for clean inflow is valid. The increase of DF due to unsteady blade loading shows only minor changes compared to the baseline cases. So, the fan has to deal with the same unsteady blade loading at a higher blade loading levels. This in turn leads to more challenging aerodynamic conditions. However, the isentropic efficiency changes are less dominant in the case of decreased solidity. Here the changed operating range prevent choking conditions in the middle of the distortion and, therefore, less changes in isentropic efficiency. So, the changes are -0.04% , -0.035% and -0.02% between the undistorted and distorted inflow conditions. Concluding from this subsection, solidity does not change the aerodynamic interaction of the fan stage with the distortion. Nevertheless, solidity remains an important design parameter for distortion tolerant fan designs a strong parameter, as solidity is the key parameter to set fan efficiency and aerodynamic blade loading.

4.5 Annulus geometry

The initial design of the DLR UHBR fan stage was dedicated to the FPR of 1.45 (see Sect. 2). Commonly, high FPRs lead to annulus designs with substantial contraction of the tip line in the rotor. In this study the fan stage is required to operate at much lower FPR in ADP. Those fan stages usually have less contraction in the rotor tip. Thus, this design sensitivity aims at reducing the contraction of the tip line as shown in Fig. 17. The red line shows the tip line of the changed flow path, which is 1% larger than in the reference flow path. Therefore, the area in this part of the flow path is changed, which coincides with a changed area ratio. This area ratio directly translates into the meridional velocity density ratio (MVDR). As the area ratio increases, MVDR decreases for the updated flow path. MVDR is mainly driven by decreasing meridional velocities at rotor outlet. In addition, the casing has a less curvature, which also reduces locally meridional velocities. Both effects lead to decreasing deHaller numbers and increasing DF. Consequently, this design parameter increases the blade loading at 80% span about 0.008, 0.004 or 0.001, respectively. At clean inflow conditions the changes in the annulus design cause degradations in isentropic efficiency in the range of -0.4% over -1.34% up to -1.63% with increasing tip speed. According to increased blade loading, the tip region of the fan rotor is less efficient than the baseline fan. This leads to the conclusion, that the entire annulus would need a redesign to reach a better fan performance in clean inflow conditions. Considering the total pressure distortion, the fans show mainly comparable changes of unsteady blade loading around the circumference. This leads to higher absolute values of DF near the tip and accordingly to higher aerodynamic blade loading. The changes in isentropic efficiency around the circumference are less dominant than for the baseline fans. The fan with 284 m/s tip speed loses -0.02% in is. efficiency, the fan with 307 m/s tip speed shows nearly no changes and the fan with a tip speed of 328 m/s shows an improvement of 0.02% . Nevertheless, it should be noted that the fans operated at lower fan efficiencies at clean inflow conditions. So, changing the annulus lines could lead to a lower isentropic efficiency drop, but the performance at different circumferential positions needs to be carefully traded.

4.6 Non-axisymmetric stator

The fifth parameter sensitivity deals with a non-axisymmetric stator. The flow field at the rotor outlet is inhomogeneous around the circumference and for that reason a non-axisymmetric stator appears to be beneficial. The individual shaping of the stator blades allows matching the stator LE and the inflow velocity triangle at every circumferential stator position. This kind of fan stage design is reported

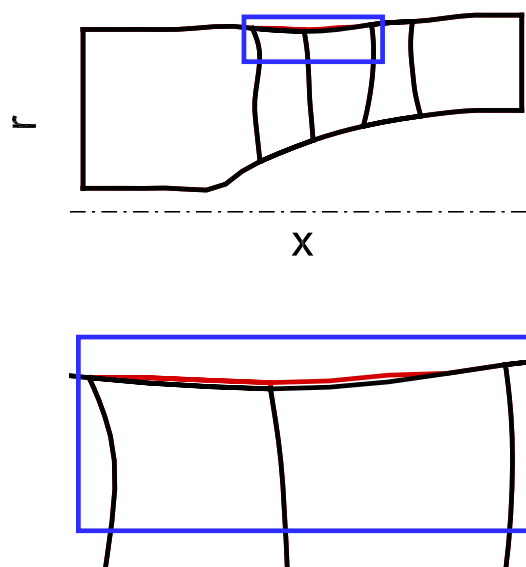


Fig. 17 Reference flow path (black) and updated flow path in the rotor tip region (red)

in literature on different levels of maturity. Hall et al. [8] applied a non-axisymmetric stator in the framework of using a body force approach. They reached the non-axisymmetric stator by individual stagger angles around the circumference. In consequence, they had to accept swirl in the flow field at the stator exit. Gunn et al. [7] designed individual stator blades by taking advantage of individual 2D airfoil design as well as individual 3D blade design (i.e. individual blade lean). The design update they presented was also subject to experimental investigations. The design intent of the updated stators is to match the stator leading edge with the inflow velocity triangle that varies around the circumference. At the stator outlet a swirl free outflow is desired. Due to the design intent the stator blades mainly differ in stagger angle and leading edge angle. Figure 18 depicts two different stator designs. One is designed for undistorted inflow conditions and one is designed for the middle of the distortion. Figure 18a shows the stator airfoils at 30% span. Those airfoils are mainly the same due to the fact that the boundary layer fluid is located in the tip region of the rotor as well as the stator. The stator airfoils at 100% span differ due to the impact of the boundary layer fluid (Fig. 18b). The shape of the LE and TE is fixed in the design and, therefore, the stator blades appear similar in Fig. 18c, d. Nevertheless there are changes which are mentioned above. Other 3D blade design features as non-axisymmetric lean cannot be taken into account in the 2D E-SLC and is beyond the scope of this paper. Nevertheless, a 3D non-axisymmetric stator is expected to have a significant impact on the overall fan stage performance. The impact of individual stator designs differs for the different tip speeds. At higher tip speeds the local operating point

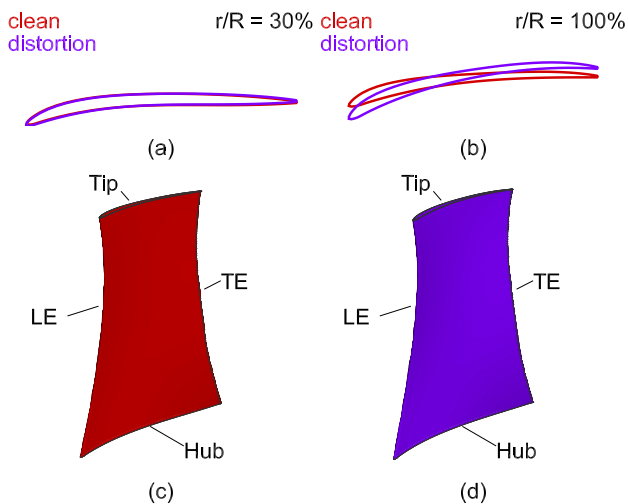


Fig. 18 Non-axisymmetric stator design. The subplots **a** and **b** show airfoils at different spanwise positions for clean inflow and the middle of distortion. Complete stator blade for a clean passage (**c**) and the middle of the distortion (**d**)

excursion is lower due to the steeper characteristic. Therefore, the impact of individual stator blades decreases with increasing tip speed. The changes in rotor performance due to the non-axisymmetric stator are quite small and mainly driven by the different tip speeds. There are minor changes in fan performance due to changes in rotor backpressure, which is imposed by individual stator blades. The changes in rotor backpressure lead to changes of the velocity field and, therefore, affect the stator incidence along the span. Figure 19 shows the loss coefficient of the axisymmetric stator in clean inflow conditions (red dashed line) and distorted inflow (red solid line) as well as the individual stator blade for distorted inflow (purple solid line). Inside the distortion (above 50% span) the axisymmetric stator shows increased losses. The loss level can be reduced by applying an individual stator blade for the middle of the distortion. Near the hub the individual stator shows higher losses than the axisymmetric blade. The main message of this sensitivity is, that using the methodology the stator performance can be improved in the region of the distortion. Nevertheless, designing an individual stator blade, which shows lower losses over the entire span is a challenge for future distortion tolerant fan designs.

5 Conclusion

In the current study, the DLR UHBR fan stage is investigated for clean and BLI inflow using high fidelity 3D CFD as well as the new design methodology 2D E-SLC. The main results are:

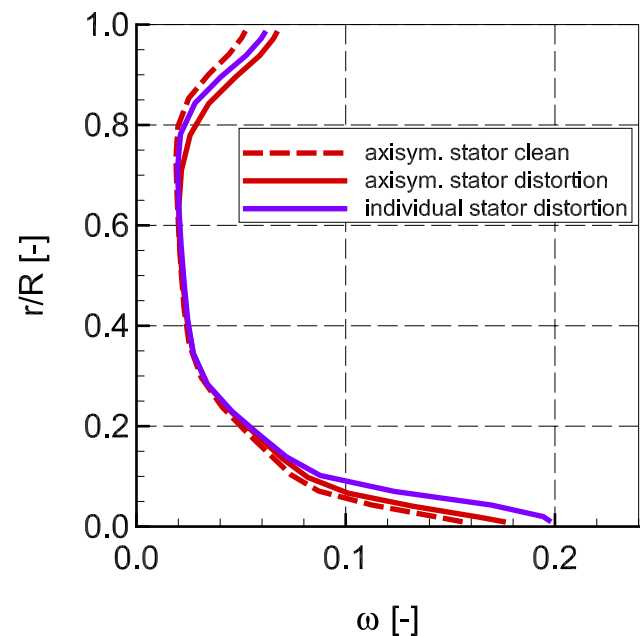


Fig. 19 Spanwise loss coefficient of an axisymmetric stator in clean inflow (red dashed line), an axisymmetric stator (red solid line) in distorted inflow and an individual designed stator for distorted inflow (purple solid line)

1. The flight conditions of an operating point largely affect the distortion pattern. Low speed and low altitude lead to more uniform distortion patterns than high speed and high altitude points.
2. Increasing severity of the distortion leads to higher levels of distortion-fan interaction. Therefore, the operating point shift increases.
3. Increasing tip speed leads to lower changes in the operating point as observed in TOC compared to CR.

On pre-design level the following results complement the high-fidelity study:

4. Increasing tip speed shows the ability to reduce unsteady blade loading as well as isentropic efficiency changes around the circumference on the expense of lower isentropic efficiency at clean inflow.
5. If increased blade thicknesses are required from structural perspective, a database of optimized airfoils can be taken advantage of to limit the efficiency degradation.
6. Solidity remains a powerful design parameter but has no further implications in BLI conditions than in clean inflow conditions.
7. A non-axisymmetric stator is able to significantly reduce losses in the tip region of the blade. The hub flow needs further attention to end up with an entirely improved stator blade.

All in all, tip speed is the most powerful parameter and distortion tolerant fans will need to be designed at higher tip speeds than conventional fans. In the future work the design methodology will be used to combine beneficial design parameters and assess the resulting fan stage on the one hand with the 2D E-SLC approach and on the other hand with a high-fidelity 3D CFD approach.

Acknowledgements The HYPER-F project leading to this application has received funding from the Clean Sky 2 Joint Undertaking (JU) under the European Union's Horizon 2020 research and innovation programme under Grant Agreement Number 807097.

Disclaimer The results, opinions, conclusions, etc. presented in this work are those of the authors only and do not necessarily represent the positions of the JU; the JU is not responsible for any use made of the information contained herein.



Author Contributions Conceptualization: MM, RS and DS; methodology: MM and MS; formal analysis and investigation: MM; writing—original draft preparation: MM; writing—review and editing: all authors; resources: MS; supervision: RS.

Funding Open Access funding enabled and organized by Projekt DEAL. The present study was realized within the scope of the HYPER-F project, which received funding from the Clean Sky 2 joint Undertaking under the European Union's Horizon 2020 research and innovation program (Grant Agreement Number 807097).

Declarations

Conflict of interest Not applicable.

Availability of data and material Not applicable.

Code availability Not applicable.

Open Access This article is licensed under a Creative Commons Attribution 4.0 International License, which permits use, sharing, adaptation, distribution and reproduction in any medium or format, as long as you give appropriate credit to the original author(s) and the source, provide a link to the Creative Commons licence, and indicate if changes were made. The images or other third party material in this article are included in the article's Creative Commons licence, unless indicated otherwise in a credit line to the material. If material is not included in the article's Creative Commons licence and your intended use is not permitted by statutory regulation or exceeds the permitted use, you will need to obtain permission directly from the copyright holder. To view a copy of this licence, visit <http://creativecommons.org/licenses/by/4.0/>.

References

1. Smith, A.M.O., Roberts, H.E.: The jet airplane utilizing boundary layer ingestion for propulsion. *J. Aeronaut. Sci.* **14**(2), 97–109 (1947)
2. Plas, A.P., Sargeant, M.A., Madani, V., Crichton, D., Greitzer, E.M., Hynes, T.P., Hall, C.A.: Performance of a boundary layer ingesting (BLI) propulsion system. In: 45th AIAA Aerospace Sciences Meeting and Exhibit, Reno. AIAA 2007-2450 (2007)
3. Sato, S.: The Power Balance Method for Aerodynamic Performance Assessment. Ph.D. Thesis, Massachusetts Institute of Technology, Cambridge (2012)
4. Gunn, E.J., Hall, C.A.: Aerodynamics of boundary layer ingesting fans. In: Proceedings of ASME Turbo Expo, Dusseldorf, GT2014-26142 (2014)
5. Gunn, E.J., Hall, C.A., Tooze, S.E., Colin, Y.: An experimental study of loss sources in a fan operating with continuous inlet stagnation pressure distortion. *J. Turbomach.* **135**(5), 051002 (2013)
6. Perovic, D., Hall, C.A., Gunn, E.J.: Stall inception in a boundary layer ingesting fan. In: Proceedings of ASME Turbo Expo 2015, Montreal, GT2015-43025 (2015)
7. Gunn, E.J., Hall, C.A.: On-axisymmetric stator design for boundary layer ingesting fans. In: Proceedings of ASME Turbo Expo, Charlotte, GT2017-63082 (2017)
8. Hall, D.K., Greitzer, E.M., Tan, C.S.: Analysis of fan stage conceptual design attributes for boundary layer ingestion. *ASME J. Turbomach.* **139**, 071012 (2017)
9. Hughes, C.E.: Aerodynamic performance of scale-model turbofan outlet guide vanes designed for low noise. In: AIAA, Reno, AIAA 2002-0347 (2002)
10. Defoe, J.J., Hall, D.K.: Fan performance scaling with inlet distortions. In: Proceedings of ASME Turbo Expo, Seoul, South-Korea, GT2016-58009 (2016)

11. Schoenweitz, D., Theune, M., Schnell, R.: Inlet distortion sensitivity of fans with different pressure ratios. In: 22nd ISABE Conference, Phoenix, ISABE-2015-20095 (2015)
12. Cousins, W.T., Voytovych, D., Tillman, G., Gray, E.: Design of a distortion-tolerant fan for a boundary layer ingesting embedded engine application. In: 53rd AIAA/SAE/ASEE Joint Propulsion Conference, Atlanta, AIAA 2017-5042 (2017). <https://doi.org/10.2514/6.2017-5042>
13. Arend, D.J., Wolter, J.D., Hirt, S.M., Provenza, A.J., Gazzaniga, J.A., Cousins, W.T., Hardin, L.W., Sharma, O.P.: Experimental evaluation of an embedded boundary layer ingesting propulsor for highly efficient subsonic cruise aircraft. In: 53rd AIAA/SAE/ASEE Joint Propulsion Conference, Atlanta, AIAA 2017-5041 (2017). <https://doi.org/10.2514/6.2017-5041>
14. Hirt, S.M., Arend, D.J., Wolter, J.D., Johnson, A.: Development of a flow field for testing a boundary-layer-ingesting propulsor. In: 53rd AIAA/SAE/ASEE Joint Propulsion Conference, Atlanta, AIAA 2017-5043 (2017). <https://doi.org/10.2514/6.2017-5043>
15. Pardo, A.C., Hall, C.A.: Aerodynamics of boundary layer ingesting fuselage fans. In: 24th ISABE Conference, Canberra, GT2019-90257 (2019)
16. Mårtensson, H., Laban, M.: Design and performance of a boundary layer ingesting fan. In: Proceedings of ASME Turbo Expo, Virtual, Online, GT2020-15479 (2020)
17. Defoe, J., Spakovszky, Z.: Effects of boundary-layer ingestion on the aero-acoustics of transonic fan rotors. *ASME J. Turbomach.* **135**, 051013 (2013)
18. Romani, G., Ye, Q., Avallone, F., Ragni, D., Casalino, D.: Numerical analysis of fan noise for the NOVA boundary-layer ingestion configuration. *Aerosp. Sci. Technol.* **96**, 105532 (2019)
19. Silberhorn, D., Eichner, F., Hollmann, C., Mennicken, M., Stagat, M.: Overall design and assessment of aircraft concepts with boundary layer ingesting engines. Deutsche Gesellschaft für Luft- und Raumfahrt-Lilienthal-Oberth e.V. (2019)
20. Hollmann, C., Schönweitz, D., Wolters, F., Otten, T.: Evaluation of boundary layer ingestion on propulsion level by coupling of overall system analysis and high-fidelity 3D-CFD fan simulation. Deutsche Gesellschaft für Luft- und Raumfahrt-Lilienthal-Oberth e.V. (2019)
21. Burak, K.: Design of an advanced fan stage with ultra high bypass ratio and comparison with experimental results. Ph.D. Thesis, Ruhr-Universität Bochum, Deutsches Zentrum für Luft- und Raumfahrt e.V., Forschungsbericht 2010-20 (2010)
22. Schnell, R., Giebmanns, A., Nicke, E., Dabrock, T.: Aerodynamic analysis of a fan for future ultra high-bypass-ratio aero engines. In: 19th ISABE Conference, Montreal, ISABE 2009-1149 (2009)
23. Wilcox, D.: Reassessment of the scale determining equation for advanced turbulence models. *AIAA J.* **26**, 1299–1310 (1988)
24. Bardina, J., Ferziger, J.H., Rogallo, R.S.: Effect of rotation on isotropic turbulence: computation and modelling. *J. Fluid Mech.* **154**, 321–336 (1993)
25. Kato, M., Launder, B.E.: The modeling of turbulent flow around stationary and vibrating square cylinders. In: 9th Symposium on Turbulent Shear Flows, pp. 10.4.1–10.4.6 (1993)
26. Becker, K., Heitkamp, K., Kügeler, E.: Recent progress in a hybrid-grid CFD solver for turbomachinery flows. In: Proceedings of Fifth European Conference on Computational Fluid Dynamics ECCOMAS CFD 2010 (2010) (ISBN: **978-989-96778-1-4**)
27. Cumpsty, N.: Compressor Aerodynamics. Krieger Publishing Company (2004) (ISBN **1-57542-247-8**)
28. Yang, H., Nurnberger, D., Weber, A.: A conservative zonal approach with applications to unsteady turbomachinery flows, DGLR-2002-073 (2002)
29. Seitz, A., Hübner, A., Risse, K.: Das DLR Projekt TuLAM—Entwurf einer Flugzeugs mit vorwärts gefeilttem Laminarflügel, Deutsche Gesellschaft für Luft- und Raumfahrt—Lilienthal-Oberth e.V. (2017)
30. DLR Institute of Aerodynamics and Flow Technology, Department Transport Aircraft
31. Mennicken, M., Schoenweitz, D., Schnoes, M., Schnell, R.: Conceptual fan design for boundary layer ingestion. In: Proceedings of ASME Turbo Expo, Phoenix, GT2019-90257 (2019)
32. Schnoes, M., Nicke, E.: A database of optimal airfoils for axial compressor throughflow design. *ASME J. Turbomach.* **139**, 051008 (2017)
33. Schlichting, H., Gersten, K.: Grenzschicht-Theorie, vol. 10. überarbeitete Auflage. Springer (2006) (ISBN **3-540-23004-1**)
34. Eichner, F., Belz, J., Winkelmann, P., Schnell, R., Lengyel, T.: Prediction of aerodynamically induced fan blade vibration due to boundary layer ingestion. In: ETC 2019—13th European Turbomachinery Conference, 08.–12. Apr. 2019, Lausanne, Schweiz (2019)

Publisher's Note Springer Nature remains neutral with regard to jurisdictional claims in published maps and institutional affiliations.